Supporting Information

Lattice dynamics of layered kagome lattice material Nb_3Br_8 investigated via Raman spectroscopy and DFT

Dylan A. Jeff[1,2,†], Ravinder Sharma[1,2,†], Gabriel Marciaga[1,2], Favian Gonzalez[1,2], Kamal Harrison[1,2], Yuzhou Zhao[3,4], Tharindu Fernando[4], Madhab Neupane[1], Jihui Yang[3], Jiun-Haw Chu[4], Xiaodong Xu[3,4], Ting Cao[3], Saiful I. Khondaker[1,2*]

[1]Department of Physics, University of Central Florida, Orlando, Florida 32816, United States
[2]NanoScience Technology Center, University of Central Florida, Orlando, FL 32826, USA
[3]Department of Materials Science and Engineering, University of Washington, Seattle, WA 98195, USA
[4]Department of Physics, University of Washington, Seattle, WA 98195, USA
†These authors contributed equally to this work
*Author to whom any correspondence should be addressed

E-mail: saiful@ucf.edu

Keywords: 2D material, topological material, kagome lattice, phonon, density-functional theory

Section 1: Raman tensor and derivation of the light-polarization equations for the different Raman mode intensities for bulk Nb$_3$Br$_8$

Mode	A$_{1g}$	E$_{g,1}$	E$_{g,2}$
R	$\begin{pmatrix} a & 0 & 0 \\ 0 & a & 0 \\ 0 & 0 & b \end{pmatrix}$	$\begin{pmatrix} c & 0 & 0 \\ 0 & -c & d \\ 0 & d & 0 \end{pmatrix}$	$\begin{pmatrix} 0 & -c & -d \\ -c & 0 & 0 \\ -d & 0 & 0 \end{pmatrix}$

Table S1. Raman tensor for Nb3$_3$Br$_8$, a crystal with point group D$_{3d}$.

Consider the Raman intensity (I) in backscattering geometry: $I \propto \left|\hat{e}_i^{\dagger}\cdot R\cdot\hat{e}_s\right|^2$. The Raman tensors (R = $R_{A_{1g}}, R_{E_{g,1}}, R_{E_{g,2}}$) correspond to the irreducible representations of crystal point group D3d and the polarization vectors of the incident and scattered light $\hat{e}_i^{\dagger}$ and $\hat{e}_s$ are defined as $\hat{e}_i^{\dagger} = \begin{pmatrix} sin(\theta+\phi) & \cos(\theta+\phi) & 0 \end{pmatrix}$ and $\hat{e}_s = \begin{pmatrix} sin\phi \\ cos\phi \\ 0 \end{pmatrix}$. ϕ is the fixed but unknown angle between the scattered polarization vector and the crystallographic b-axis and θ is the polarization angle, defined as the angle between the incident and scattered polarization vectors. Here rotating θ defines the polarization configuration (e.g., parallel or crossed) and the angle ϕ accounts for the orientation relative to the crystal axes.

1. For A$_{1g}$ modes:

$$I_{A_{1g}} \propto \left|\hat{e}_i^{\dagger}\cdot R_{A_{1g}}\cdot\hat{e}_s\right|^2 \propto \left|\begin{pmatrix} \sin(\theta+\phi) & \cos(\theta+\phi) & 0 \end{pmatrix}\begin{pmatrix} a & 0 & 0 \\ 0 & a & 0 \\ 0 & 0 & b \end{pmatrix}\begin{pmatrix} sin\phi \\ \cos\phi \\ 0 \end{pmatrix}\right|^2 \propto$$

$$\left|\begin{pmatrix} a\sin(\theta+\phi) & a\cos(\theta+\phi) & 0 \end{pmatrix}\begin{pmatrix} \sin(\phi) \\ \cos(\phi) \\ 0 \end{pmatrix}\right|^2 \propto$$

$$\left|asin(\theta+\phi)sin\phi + a\cos(\theta+\phi)cos\phi\right|^2 \propto \left|acos((\theta+\phi)-\phi)\right|^2$$

Therefore $I_{A_{1g}} \propto a^2cos^2(\theta)$, this is equation (2) in the manuscript.

1.1 For parallel polarization, $\theta = 0$:

$$I_{A_{1g}}^{\parallel} \propto \left|acos0\right|^2 \propto a^2$$

1.2 For cross-polarization $\theta = 90$:

$$I_{A_{1g}}^{\perp} \propto \left|acos^2 90\right|^2 \propto 0$$

2. For $E_{g,1}$ modes:

$$I_{E_{g,1}} \propto \left|\hat{e}_i^{\dagger} \cdot R_{E_{g,1}} \cdot \hat{e}_s\right|^2 \propto \left|\begin{pmatrix} sin(\theta+\phi) & cos(\theta+\phi) & 0 \end{pmatrix}\begin{pmatrix} c & 0 & 0 \\ 0 & -c & d \\ 0 & d & 0 \end{pmatrix}\begin{pmatrix} sin\phi \\ \cos\phi \\ 0 \end{pmatrix}\right|^2 \propto$$

$$\left|\begin{pmatrix} csin(\theta+\phi) & -ccos(\theta+\phi) & 0 \end{pmatrix}\begin{pmatrix} sin\phi \\ \cos\phi \\ 0 \end{pmatrix}\right|^2$$

$$I_{E_{g,1}} \propto |csin(\theta+\phi)sin\phi - ccos(\theta+\phi)cos\phi|^2 \propto |-ccos((\theta+\phi)+\phi)|^2$$

$$\propto |ccos(\theta+2\phi)|^2$$

Therefore $I_{E_{g,1}} \propto c^2cos^2(\theta+2\phi)$.

2.1 For parallel polarization ($\theta = 0$)

$$I_{E_{g,1}}^{\parallel} \propto c^2cos^2(0+2\phi) \propto c^2cos^2(2\phi)$$

2.2 For cross-polarization ($\theta = 90$):

$$I_{E_{g,1}}^{\perp} \propto c^2cos^2(90+2\phi)$$

3. For $E_{g,2}$ modes:

$$I_{E_{g,2}} \propto \left|\hat{e}_i^{\dagger} \cdot R_{E_{g,1}} \cdot \hat{e}_s\right|^2 \propto \left|\begin{pmatrix} \sin(\theta+\phi) & \cos(\theta+\phi) & 0 \end{pmatrix}\begin{pmatrix} 0 & -c & -d \\ -c & 0 & 0 \\ -d & 0 & 0 \end{pmatrix}\begin{pmatrix} sin\phi \\ \cos\phi \\ 0 \end{pmatrix}\right|^2 \propto$$

$$\left|\begin{pmatrix} -ccos(\theta+\phi) & -csin(\theta+\phi) & 0 \end{pmatrix}\begin{pmatrix} sin\phi \\ \cos\phi \\ 0 \end{pmatrix}\right|^2 \propto$$

$$|-ccos(\theta+\phi)sin\phi - csin(\theta+\phi)cos\phi|^2 \propto |-csin((\theta+\phi)+\phi)|^2 \propto$$

$$|-csin(\theta+2\phi)|^2$$

Therefore $I_{E_{g,2}} \propto c^2sin^2(\theta+2\phi)$

3.1 For parallel polarization, $\theta = 0$:

$$I_{E_{g,2}}^{\parallel} \propto c^2sin^2(0+2\phi) \propto c^2sin^2(2\phi)$$

3.2 For cross-polarization $\theta = 90$:

$$I_{E_{g,2}}^{\perp} \propto c^2sin^2(90+2\phi)$$

For a generalized expression considering both E_g modes, we define:

$I_{E_g} \propto I_{E_{g,1}} + I_{E_{g,2}} \propto c^2cos^2(\theta+2\phi) + c^2sin^2(\theta+2\phi)$, this is equation (3) in the manuscript.

Section 2: Excitation-dependent Raman spectroscopy of Nb_3Br_8

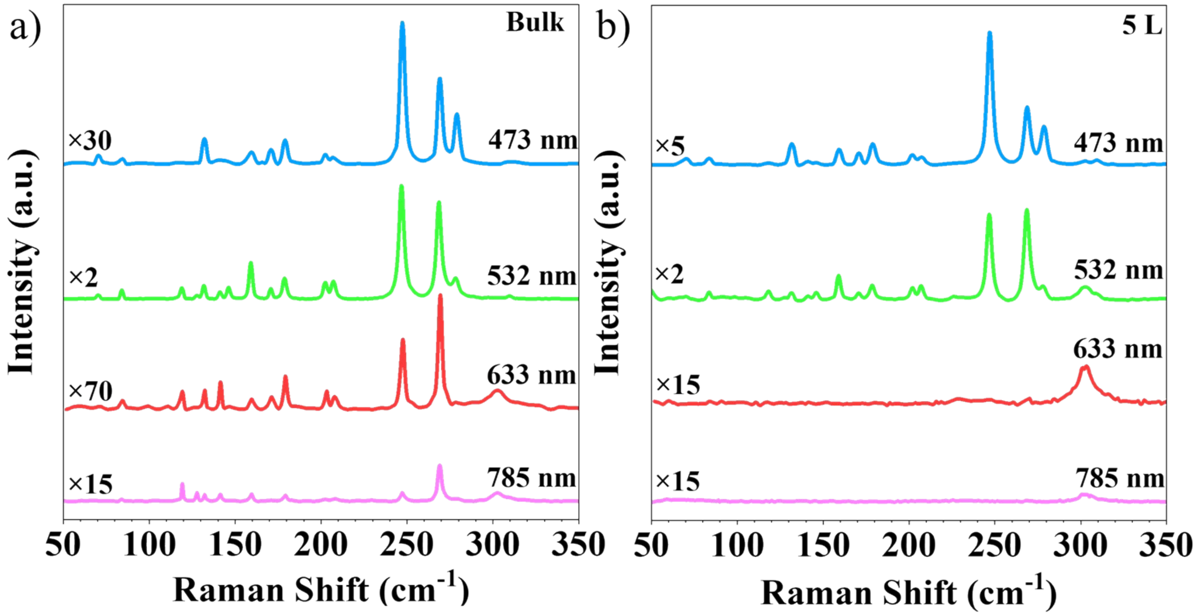

Figure S1. Excitation-dependent Raman spectra of (a) exfoliated bulk and (b) 5L Nb_3Br_8 crystal taken with 473, 532, 633, and 785 nm excitation sources. Each curve is multiplied to discern the number of resolvable peaks according to the excitation source used. Using a 532 nm excitation source on a bulk (204 L) sample provided the best peak resolution. The extra peaks resolved with the 532 nm laser indicates the presence of a near-resonance effect where resonance Raman scattering occurs due to the incident energy event matches the energy of an electronic transition within the material. This resonance typically results in increased Raman mode intensities, serving as an interaction that assists in resolving as many Raman modes as possible, regardless of the intrinsic intensity of the mode. The 532 nm source also resolved the most peaks in the 5L sample, resolving 13 peaks. Furthermore, using a 473 nm excitation source sharply resolved the peak near 279 cm^{-1}, where it appears as a shoulder when using other wavelengths, indicating resonance between the specific phonon mode and the energy of the laser.

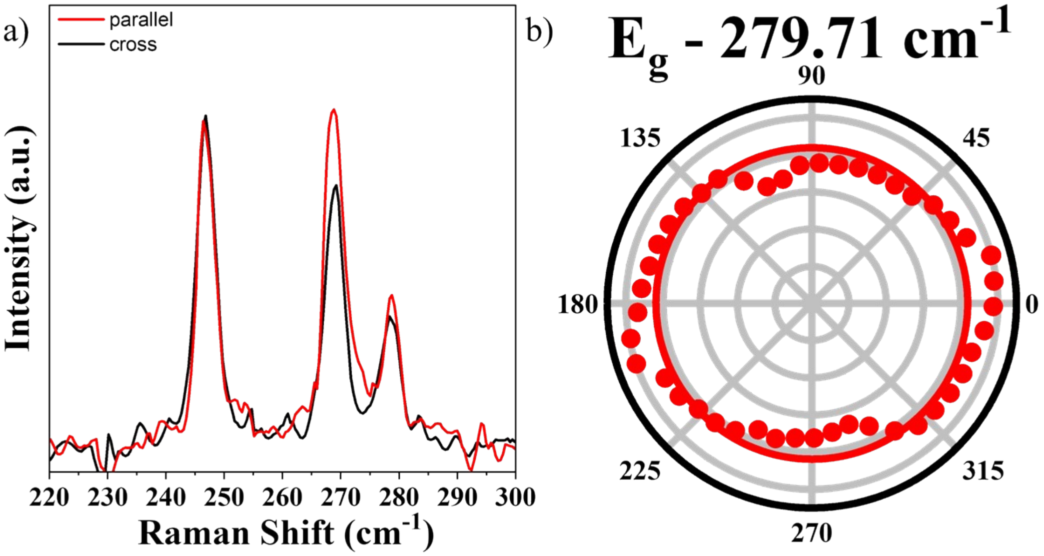

Figure S2. (a) Linearly polarized Raman spectroscopy of bulk Nb_3Br_8 with a 473 nm excitation source was performed to better resolve the polarization dependence of P17, with the red curve corresponding to parallel polarization and the black curve corresponding to cross polarization. (b) The polar plot of the peak's intensity across different polarization angles is more comparable to that of an E_g peak, as the influence of the neighboring peak is drastically reduced due to the increased resolution from the 473 nm source.

Section 3: High-Temperature Polarized Raman Spectroscopy of Nb_3Br_8

Room Temperature		**443 K**		**Δ Frequency**
Frequency [cm^{-1}]	**Irreducible Representation**	**Frequency [cm^{-1}]**	**Irreducible Representation**	**Frequency [cm^{-1}]**
19.71	E_g	18.47	E_g	1.24
43.76	A_{1g}	-	-	-
71.41	E_g	69.96	E_g	1.45
85.00	E_g	83.94	E_g	1.06
119.97	A_{1g}	118.44	A_{1g}	1.53
128.69	A_{1g}	127.00	-	1.69
132.92	E_g	130.90	E_g	2.02
141.21	A_{1g}	140.37	A_{1g}	0.84
147.19	E_g	145.48	E_g	1.71
160.19	E_g	157.95	E_g	2.24
171.74	A_{1g}	170.00	A_{1g}	1.74
179.75	E_g	177.64	E_g	2.11
203.48	A_{1g}	201.60	A_{1g}	1.88
208.32	E_g	205.31	E_g	3.01
247.94	E_g	245.08	E_g	2.86
269.68	A_{1g}	266.24	A_{1g}	3.44
279.71	E_g	276.34	E_g	3.37
310.00	A_{1g}	-	-	-

Table S2. Raman active phonon modes of bulk Nb_3Br_8 at room temperature (300 K) and 443 K. The effect of high temperature on the lattice dynamics of the Nb_3Br_8 crystal system are exemplified in the table above. The frequencies of each mode all decrease at higher temperatures as the crystal lattice expands due to heat. Regardless of the expected structural phase transition expected at temperatures higher than 393 K, no changes in phonon mode symmetry were observed at 443 K. x

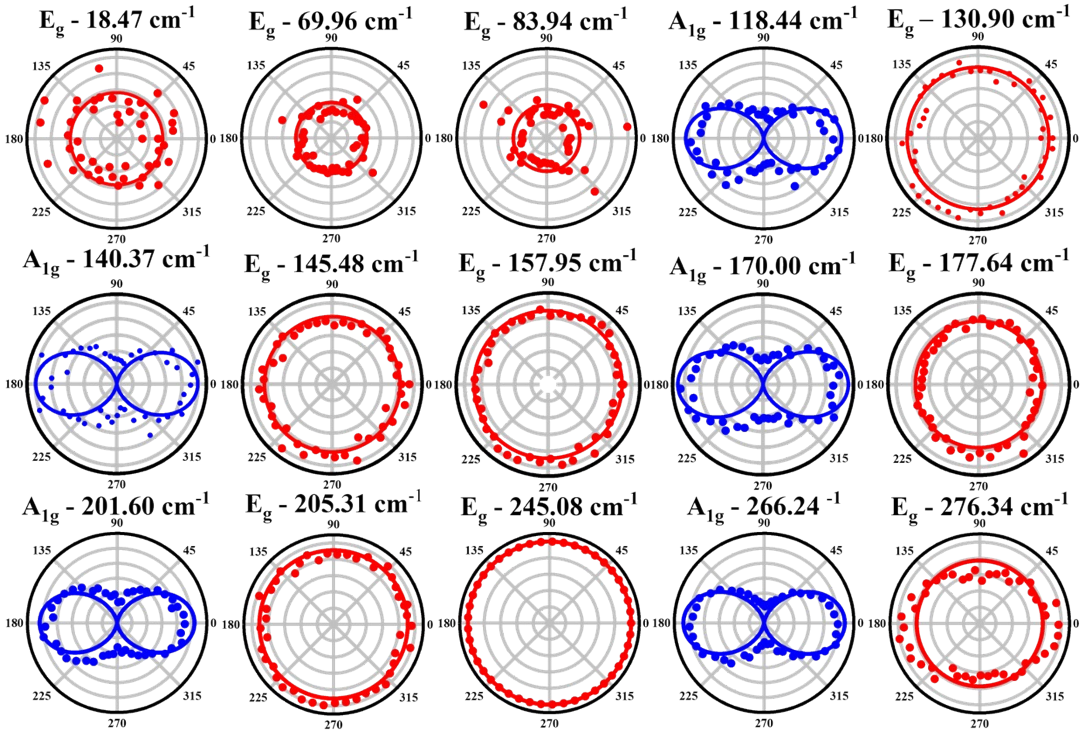

Figure S3. Linearly polarized Raman polar plots taken on bulk Nb_3Br_8 at 443 K with a 532 nm excitation source. To probe how the temperature-dependent structural phase change of Nb_3Br_8's stacking order affects the phonon dynamics of the crystal system, further angle-resolved PRS experiments were performed at 443 K, beyond the transition temperature of 393 K observed in our experiment. Aside from shifts in frequency and noisier data due to the increase in temperature, the symmetry of each peak remained consistent with their corresponding symmetries at room temperature. This indicates that the phase change that Nb_3Br_8 undergoes at high temperatures has no effect on the Raman selection rules of the phonon modes. Intensities are normalized with respect to the intensity of the consistent E_g peak at 245.08 cm^{-1}.

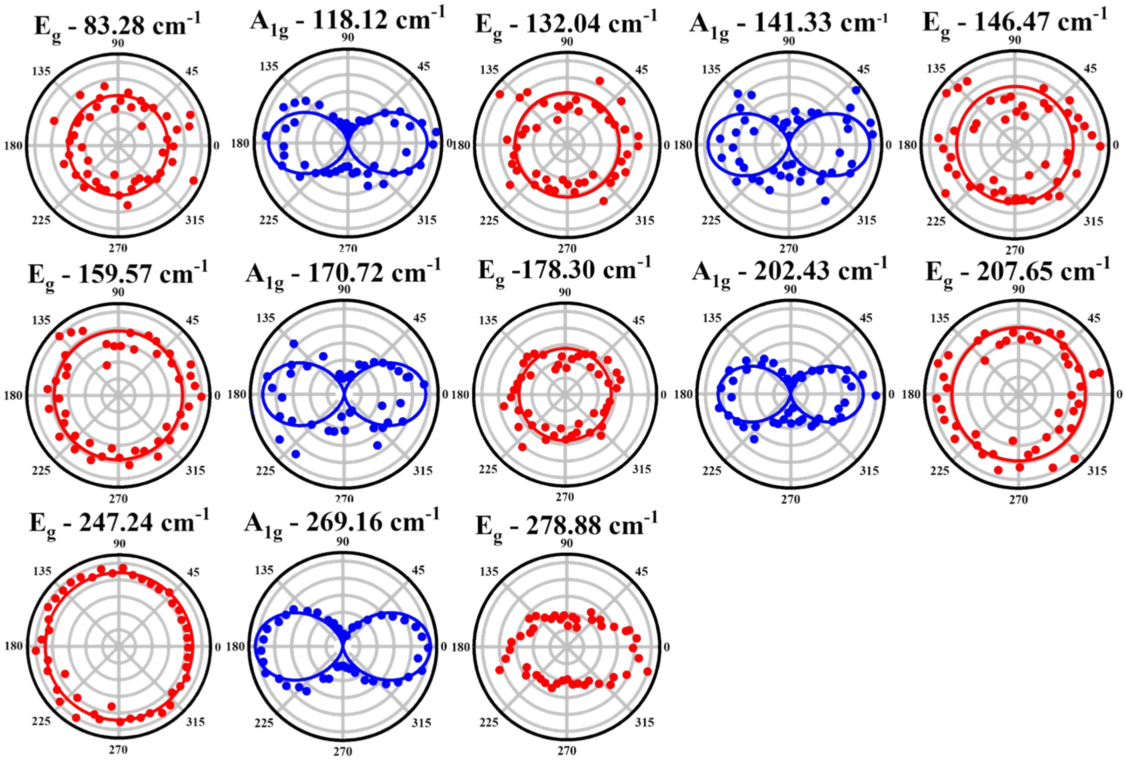

Figure S4. Linearly polarized Raman polar plots of 2L Nb_3Br_8 taken with a 532 nm excitation source at room temperature. The linearly polarized Raman study of 2L Nb_3Br_8 indicate no change in the symmetries or functional dependence of the modes when the material is thinned down to sub 2 nm thickness. The frequencies of each peak are slightly larger, as expected when thinning a 2D material due to the loss of interlayer interaction and their effects on the phonon modes of the crystal system. Furthermore, as the material is thinned, the general intensities of each peak decreases as well, resulting in worsened signal-to-noise ratios and scattered polar plots. All intensities are normalized with respect to the intensity of the constant E_g peak at 247.24 cm^{-1}.

Section 4: Layer Dependent Raman Spectroscopy of Nb_3Br_8 Thin Layers

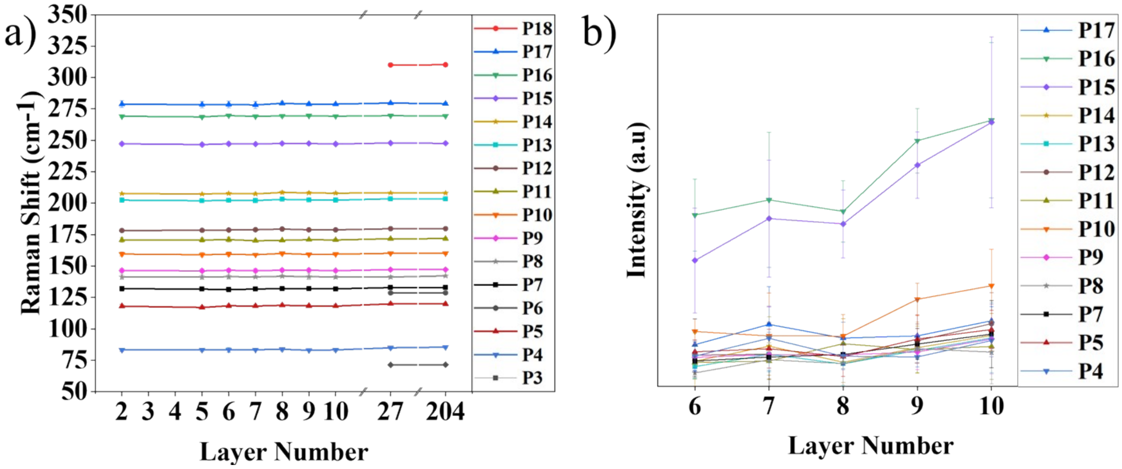

Figure S5. (a) Frequencies and (b) intensities of resolvable peaks in thin layers dependent on layer number. There are slight shifts in frequencies as the material is thinned, however all peaks remain relatively consistent. Tracking the intensity of each peak, many peaks experience a drop in intensity as the material is exfoliated down to thinner limits.

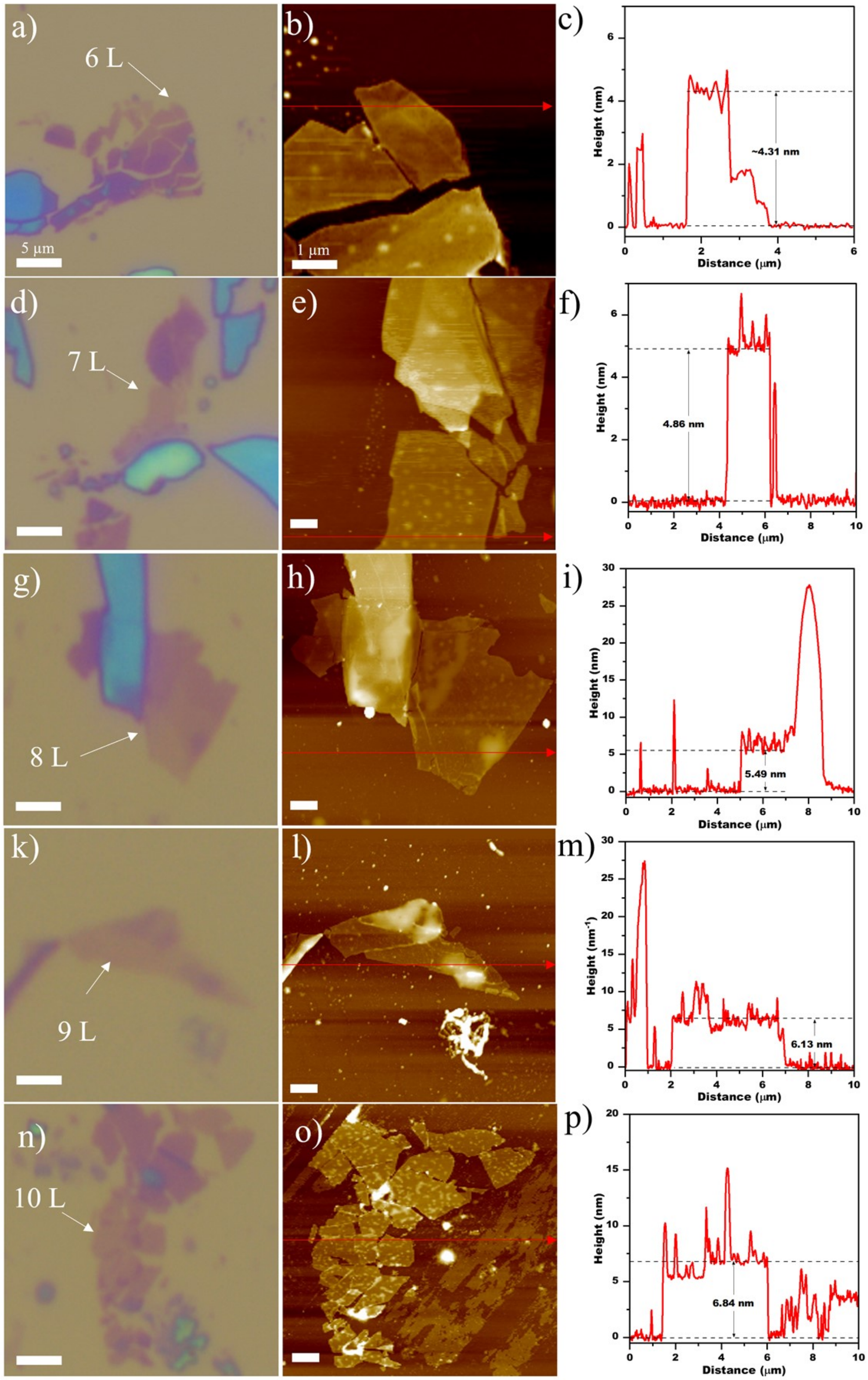

Figure S6. a) – p) Optical images, AFM images, and corresponding AFM height profiles of the Nb_3Br_8 flakes studied for layer-dependent Raman analysis. The scale bar provided in a) is applicable to all optical images and the scale bars in the AFM images are all 1 μm.

Peak Number	y-intercept	R^2
P4	17.40	0.12
P5	3.82	0.63
P7	-10.79	0.85
P8	-27.49	0.94
P9	12.41	0.60
P10	-7.69	0.68
P11	-5.04	0.71
P12	-5.56	0.89
P13	-10.03	0.81
P14	-16.16	0.64
P15	-70.76	0.86
P16	16.14	0.65
P17	6.27	0.73

Table S3. The layer dependent Raman intensities of each peak shown in Fig S5b are fitted with a linear equation. According to the fits performed on the layer-dependent data, the y-intercepts for each mode are all large, with the smallest being 3.8 for peak P5. Proportional data would feature y-intercepts close to or equal to 0. Values of $R^2 \approx 1$ signify that the data is well fitted, suggesting a linear relationship between layer number and peak intensity. R^2 is found to be above 0.6 for most of the peaks, with the highest being 0.94 for peak P8.

Section 4: Relaxed Atomic Coordinates and Wyckoff Labels

Atom	Fractional Coordinates (x,y,z)	Wyckoff	Site Symmetry
Nb	(0.14452, 0.55160, 0.55160)	h	m
Nb	(0.55160, 0.55160, 0.14452)	h	m
Nb	(0.55160, 0.14452, 0.55160)	h	m
Nb	(0.44840, 0.85548, 0.44840)	h	m
Nb	(0.85548, 0.44840, 0.44840)	h	m
Nb	(0.44840, 0.44840, 0.85548)	h	m
Br	(0.36543, 0.36543, 0.36543)	c	3m
Br	(0.63457, 0.63457, 0.63457)	c	3m
Br	(0.21391, 0.21391, 0.21391)	c	3m
Br	(0.78609, 0.78609, 0.78609)	c	3m
Br	(0.37297, 0.88194, 0.88194)	h	m
Br	(0.88194, 0.88194, 0.37297)	h	m
Br	(0.70565, 0.70565, 0.20675)	h	m
Br	(0.20675, 0.70565, 0.70565)	h	m
Br	(0.70565, 0.20675, 0.70565)	h	m
Br	(0.29435, 0.79325, 0.29435)	h	m
Br	(0.29435, 0.29435, 0.79325)	h	m
Br	(0.79325, 0.29435, 0.29435)	h	m
Br	(0.11806, 0.11806, 0.62703)	h	m
Br	(0.62703, 0.11806, 0.11806)	h	m
Br	(0.11806, 0.62703, 0.11806)	h	m
Br	(0.88194, 0.37297, 0.88194)	h	m

Table S4. Relaxed atomic coordinates, Wyckoff labels, and site symmetries used in DFT calculations.